International Refrigeration and Air Conditioning
Conference

School of Mechanical Engineering

2018

Experimental Characterization of Flow Field Around Heat Exchanger Cells in a Residential Gas Furnace

Puyuan Wu
Purdue University, wu912@purdue.edu

Weixiao Shang
Purdue University, shangw@purdue.edu

Jun Chen
junchen@purdue.edu

Experimental Characterization of Flow Field Around Heat Exchanger Cells in a Residential Gas Furnace

Puyuan Wu[1], Weixiao Shang[2], Jun Chen[3]

[1] School of Aeronautics and Astronautics, Purdue University
West Lafayette, IN, USA
wu912@purdue.edu

[2] School of Mechanical Engineering, Purdue University,
West Lafayette, IN, USA
shangw@purdue.edu

[3*] School of Mechanical Engineering, Purdue University,
West Lafayette, IN, USA
junchen@purdue.edu

* Corresponding Author

ABSTRACT

For a long time, the optimization of the design of a residential gas furnace heavily relies on CFD-based design tool. In this study, Particle Image Velocimetry (PIV) is applied to measure the flow field around heat exchanger cells in a general model of a residential gas furnace to provide benchmark validation of CFD validations. The gas furnace, combined with inlet and outlet duct and a large exhaust chamber, can simulate a set of realistic operational conditions with seeded particles circulated inside. It is discovered that strong circulation exists around the top of the cells due to flow separation. Vortex shedding from two curved end plates is also observed. The result also shows that, by changing the inlet settings, the flow field between cells may transit from symmetric to asymmetric. The detailed flow structures will help optimize the deployment of key components that was practiced before in a trial and error approach.

1. INTRODUCTION

In 2010, 45% of the residential site energy was consumed by the space heating in the US, according to the Building Energy Data by the Department of Energy (DOE) (https://catalog.data.gov). Thus, the optimization of the design of the gas furnace is important for improving efficiency and saving energy.

For a long time, engineers learn the internal flow of a residential gas furnace mainly by employing Computational Fluid Dynamics (CFD). However, there are some obstacles for employing CFD in the design: (i) fine parts exist in the gas furnace and simplification must be applied. (ii) the flow filed in an HVAC can be nonuniform (Chwalowski et al, 1989), and CFD mesh has to adopt such complicated flow field. (iii) the typical Reynolds number of the internal flow of an HVAC system can be in a critical range. (iv) the flow in an HVAC can be highly unsteady. Thus, the mesh, turbulence model and CFD method have to be validated by benchmark experiments. In the past, trial experimental methods such as transversing a hot wire anemometer or pitot tube are applied to validate CFD results. However, using the hot wire and pitot tube cannot give a flow field with high resolution and probes would affect the flow field.

Particle Image Velocimetry (PIV) is a non-invasive laser based flow diagnostic techniques and has been used to measure complicated flow field (Adrian and Westerweel, 2011; Raffel et al,2008). Repeated PIV measurements can provide high accuracy results for benchmark and statistical analysis.

Although a few examples of the application of PIV in an HVAC system are reported (Yashar and Domanski, 2009; KamijiY et al,2012), the internal flow of a residential gas furnace has never been measured by PIV, according to the best of our knowledge.
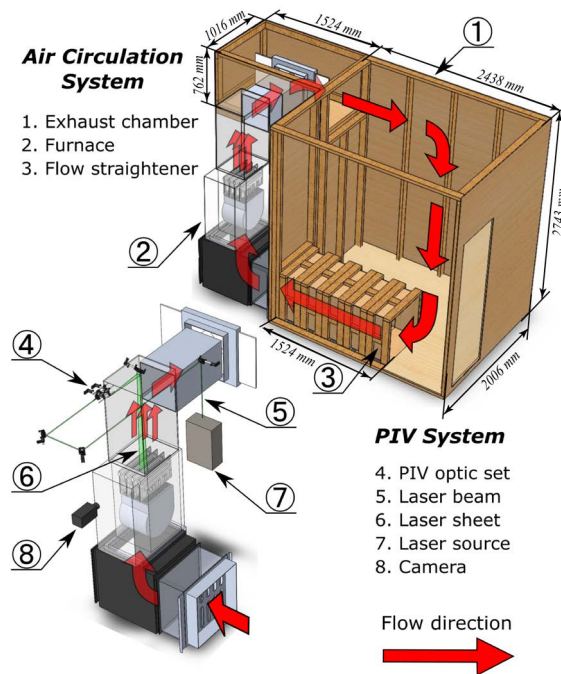
Figure 1: Schematic of the experiment setup.

The present work performs PIV experiment around the primary heat exchangers of a residential gas furnace where the flow is far from uniform and is a major concern for improving heat transfer efficiency. At the present phase, the gas burner is not working and the flow is assumed to be isotropic.

2. METHODOLOGY

2.1 EXPERIMENTAL SETUP

The experiment setup contains two independent systems: a generic gas furnace model and an air circulation system (Fig. 1). The gas furnace model (Fig. 2) has a blower, four primary heat exchangers (clamshell type, labeled as Cells #1 - #4), a secondary heat exchanger (SHE in Fig. 2), side baffles (SBL and SBR in Fig. 2) and the control electronics. The primary heat exchanger can be divided into three portions (Fig. 3). The cross section of the upper and middle portions is oval while the upper one has larger size. The cross section of the lower portion has an irregular geometry.

The air circulation system (Fig. 1) is composed by a large exhaust chamber with extension ducts, a flow straightener, side-suction inlet duct, inlet damper, base, outlet duct, outlet snout and outlet damper. The exhaust chamber and its extension has an volume of $14.6 m^3$. The flow straightener is designed by the principle of low-speed wind tunnel and has a length of $1,524\ mm$ and a cross section of $609.6 \times 609.6\ mm^2$. The flow straightener shares the same cross-section size and geometry with the inlet duct. To generate an approximate uniform flow in the inlet duct, a $101.6\ mm$ thick Polypropylene honeycomb (cell size $3.175\ mm$) and four layers of aluminum mesh screens are employed. The inlet damper can be assembled between the flow straightener and the inlet duct, and its details will be introduced in the section of experiment conditions. The outlet damper is in the chamber's extension and $406.4\ mm$ away from the end wall. Thus, the jet flow from outlet damper can develop freely before it reaching the main chamber. The opening of the outlet damper can be adjusted to meet the specific level.

To gain access to the internal flow of the furnace and its outlet duct, multiple observation windows are mounted on the furnace and the outlet ducts.
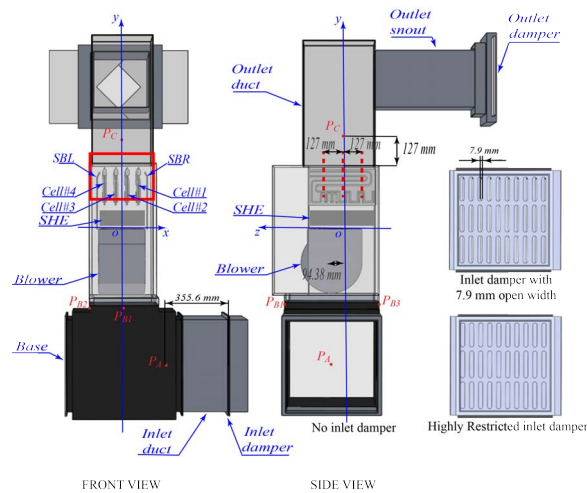
Figure 2: Measurement locations and schematic of the inlet damper. Red dashed lines: *z* locations of the three PIV measurement planes; Red rectangular: coverage zone of PIV measurement for a chosen *z* location.
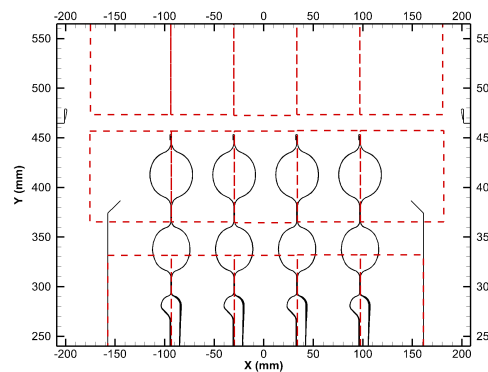

Figure 3: The layout of 15 measurement locations. The cross section of four primary heat exchangers, SBL and SBR are also indicated.

2.2 Instrumentations

Small particles with diameter of ~ 1 *μm* is generated by a heavy duty Fog Machine and vented into the chamber. A Nd:YAG double pulsed laser (532 *nm*, 200 mJ/pulse), PIV optic set and a CCD camera (double exposure, 4 Megapixels) with a 65 *mm* lens are mounted on a frame system built around the experiment set up. The optics and camera can be reconfigured on the frame system to take measurements at different target locations. The frame system is isolated from the air circulation system to prevent vibration produced by the furnace. The laser and the camera are controlled by a Programmable Timing Unit. The differential time of two pulse lasers ranges from 50 *μs* to 400 *μs* according to the estimated flow velocity.

The raw images are processed with PIV software (Davis 8.4). An initial window size of 64 × 64 pixels and 50% overlap on two directions is firstly applied and iterates for 5 times. The window size is then shrunk to 32 × 32 pixels with 50% overlap and 5 iterations. 1,000 snapshots are collected for every target location and condition to analyze statistics. Some regions in the sample area are masked out due to the blockage of structures or strong reflection in the background. The spatial resolution of velocity measurement ranges from 0.76 *mm* to 0.86 *mm*.

To obtain a nearly complete understanding of flow structure around the primary heat exchangers, PIV measurements were conducted at 15 locations by translating the laser and the camera, as denoted by the red rectangular in Fig. 3. The results from different 15 locations are patched together for the analysis.

Table 1: Experiment Conditions

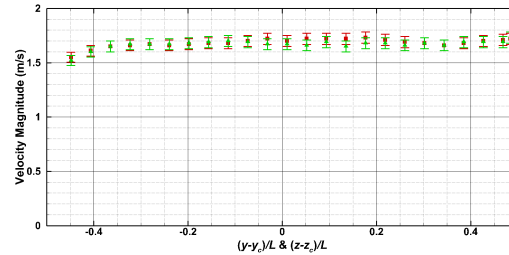| #	Case Description	$P_A - P_{atm}$ (Pa)	$P_B - P_{atm}$ (Pa)	$P_C - P_{atm}$ (Pa)	$P_C - P_B$ (Pa)	Blower Speed (rpm)
1	No Damper	-15.0	-17.4	12.5	29.9	850
2	Open Damper	-239.1	-226.7	7.5	234.1	1,110
3	Highly Restricted Damper	-418.4	-401.0	0	401.0	1,193

[1] P_{atm} is the atmospheric pressure.

Figure 4: Profiles of velocity amplitudes upstream of the inlet duct, measured by hot-wire anemometer at 254 mm from the inlet (no damper case). Green symbols: profile along the horizontal centerline; Red symbols: profile along the vertical centerline. Error bars indicate the measurement uncertainty. (y_c, z_c) is the center of the cross-section. $L = 609.6$ *mm* is the width of the inlet duct.

The air pressure at three control points (A, B, and C as labeled in Fig. 2) is measured by an incline manometer and a digital manometer. The rotation speed of the furnace blower is measured with a laser tachometer.

2.3 Experiment Conditions

The measurements are conducted under three sets of conditions, to simulate three characteristic operation cases of a residential gas furnace. These conditions are prescribed by the pressure measurements, as shown in Tab. 1. Case 1 represents a maximum flow scenario in routine furnace operations. In this case, there is no damper set attached to the inlet duct and the test aims to evaluate the maximum flow rate in an ideal laboratory condition. Case 2 simulates the scenario by attaching an inlet damper (Fig. 2), which introduces a significant duct or filter restriction but the furnace should still operate indefinitely within temperature limits. In case 3, a highly restricted inlet damper applies a severe blockage. In these three cases, the characteristic pressure differences between the furnace outlet and inlet, $P_C - P_A$, are maintained at 29.9 Pa, 234.1 Pa, and 401.0 Pa, respectively. In the following analysis, these three cases are referred to as "*no damper case*", "*open damper case*", and "*highly restricted damper case*", respectively. One is reminded that, in the highly restricted damper case, there is still weak flow circulating in the system although its features are much more complicated than the other two cases.

The coordinate system is defined in Fig. 2. The XY plane is the vertical plane 94.38 mm away from the axis of the blower. The three planes of PIV measurements, paralleling to XY plane, are $Z = 127$ *mm*, $Z = 0$ *mm* and $Z = -127$ *mm*, respectively, as shown in Fig. 2.

Fig. 4 characterizes the profiles of the air flow (along Y and Z directions, respectively) upstream of the inlet duct (in the flow straighter) for the no damper case. The profiles are nearly uniform, with an average value of 1.70 *m/s*.

3. RESULTS AND DISSCUSSIONS

PIV measurements yield the velocity, $U_i(\mathbf{x}, t)$, in the sample volume. Fig. 5 presents one characteristic snapshot. The ensemble-averaged velocity at a location $\mathbf{x}$ is computed by

$$\overline{U}_i(\mathbf{x}) = \frac{1}{N} \sum_{n=1}^{N} U_i(\mathbf{x}, t_n), \tag{1}$$
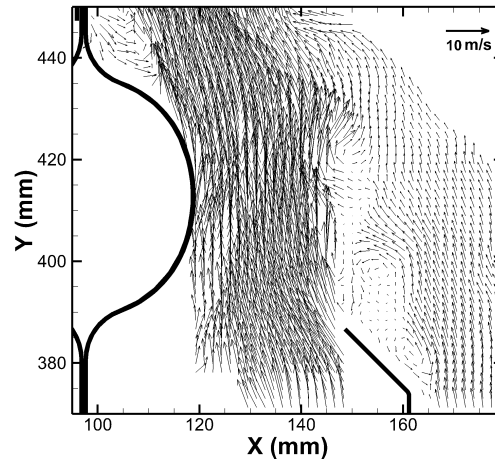
Figure 5: A instantaneous PIV measurement a $z = -127$ *mm* **in the no damper case. Time interval between the two laser pulses is** $\delta t = 50$ μs**. Only 1/4 of the vectors are plotted for clarity of display. Also shown are a portion of the primary heat exchanger and the side baffle.**

Where $U_i(\mathbf{x}, t_n)$ is the measured velocity component along direction x_i at $\mathbf{x}$ and time t_n. N is the total number of snapshots (N=1,000). The velocity fluctuation is characterized by the RMS value

$$u_i(\mathbf{x}) = \sqrt{\frac{1}{N}\sum_{n=1}^{N}\left[U_i(\mathbf{x}, t_n) - \overline{U}_i(\mathbf{x})\right]^2}. \tag{2}$$

Furthermore, by assuming isotropy, the missing RMS values in the out-of-plane direction can be estimated by the two measured in-plane components, i.e., $u_3^2 \simeq \frac{1}{2}(u_1^2 + u_2^2)$. Thus, the turbulence kinetic energy (TKE) can be estimated by

$$k(\mathbf{x}) = \frac{1}{2}\left(u_1^2 + u_2^2 + u_3^2\right) \simeq \frac{3}{4}(u_1^2 + u_2^2). \tag{3}$$

A conservative estimation of the error of an instantaneous PIV measurement is 0.1 pixels for a PIV processing algorithm. The statistical analysis shows that the characteristic displacements are 10 pixels for no damper case and open damper case and 3 pixels for highly restricted damper case. Thus, the characteristic relative error of instantaneous velocity is 1% for no damper case and open damper case, and 3.3% for highly restricted damper case. The error analysis then gives the error of the mean velocity is 0.03% for no damper case and open damper case and 0.1% for highly restricted damper case. For 1000 snapshots, the relative uncertainty of the RMS of velocities is 2.2% for three cases. With the assumption of isotropy and u_1 equals u_2, the relative uncertainty of TKE is 2.6% for three cases.

3.1 No Damper Case
When there is no inlet damper installed in the setup, the averaged velocity (*X*-component and *Y*-component) and TKE of three *Z* planes, as shown in Fig. 6, display nearly symmetric pattern with respect to the central plane (*X*=2 mm) of four primary heat exchangers. In addition, the flow patterns in three *Z* planes are similar. One is reminded that the irregular void areas between primary heat exchangers, SBL and SBR in Fig. 6(A-C) are due to the strong reflection from the background, where no meaningful particle images can be retrieved for PIV processing.

For the flow field under $Y = 350$ *mm*, the flow is straightly upward between primary heat exchangers while the flow between SBL and Cell#4, as well as the flow between SBR and Cell#1 are towards two side baffles, respectively. $\overline{U}_x$ and k keep at a low value of -1 to 1 *m/s* (Fig. 7G) and 0 to 6 m^2/s^2 (Fig. 7I), respectively. Meanwhile, $\overline{U}_y$ ranges from 2 to 9 *m/s* before reaching the middle portion of cells (Fig. 7H).

In the region between $Y = 370$ *mm* and $Y = 460$ *mm*, the flow separates from the upper portion of primary heat exchangers after passing the minimum interval of two adjacent cells at $Y = 415$ *mm* where $\overline{U}_y$ also reaches its maximum value of 15*m/s*. The flow then becomes a turbulent jet that has a maximum k exceeding 20 m^2/s^2 (Fig. 7F), suggesting

a complicated separation and entrainment process above the upper portion of the cells. Separation bubbles are formed at each side of the split plates. The flow developing from SBL and SBR are towards Cell#1 and Cell#4 due to the curvature of side baffles and the maximum $\bar{U}_x$ of 6 m/s is at the tip of two side baffles. Meanwhile, $\bar{U}_y$ accelerates to 15 m/s after detaching from SBL and SBR (Fig. 7E). The high k region developing from SBL and SBR has a uniform value of 15 m^2/s^2 and is generated by the vortex shedding from the tip of two side baffles. Although reverse flow is observed at the left side of $Z = 127$ mm plane and both sides of $Z = 0$ mm plane, the mean velocity (*X*-component and *Y*-component) and TKE are much lower comparing with the flow between SBL and SBR and are −1 to 1 m/s, −3 to 3 m/s and 0 to 5 m^2/s^2 respectively.

The outlet duct is above $Y = 465$ mm. The flow moves upward in the center of the duct and reverse flow is observed at two sides in all three *Z* planes. $\bar{U}_x$ ranges from −1 to 1 m/s except the flow developing from SBL and SBR that has a magnitude of 4 m/s (Fig. 7A). $\bar{U}_y$ decelerates to $3m/s$ to $10m/s$ for all three *Z* planes (Fig. 7B). The maximum k at outlet at $Z = 127$ mm, $Z = 0mm$, $Z = −127mm$ planes are 6 m^2/s^2, 17 m^2/s^2 and 12 m^2/s^2 (Fig. 7C), respectively. The difference could be the result of the asymmetric structure of the exit of the blower. Also, in the outlet duct, the flow developing from two side baffles tends to have higher k than the flow field above Cell#2 and Cell#3 for $Z = 0$ mm and $Z = −127$ mm plane (Fig. 7C).

3.2 Open Damper Case

For this case, the mean velocity of three *Z* planes (Figs. 8ABDEGH) are symmetric and show similar characteristics. The streamline and $\bar{U}_x$ and k under $Y = 350$ mm are similar to those in the no damper case (Fig. 9GI). $\bar{U}_y$ ranging 3 to 7.5 m/s (Fig. 9H) has lower peak value than that in no damper case.

The flow between $Y = 370$ mm to $Y = 460$ mm also shows similar streamlines with that in the no damper case. Separation is again observed at the minimum interval of the upper portion of two adjacent cells at $Y = 415$ mm but with a lower value of 11 m/s. $\bar{U}_x$ at the tip of two side baffles has its maximum magnitude of 5 m/s. $\bar{U}_x$ then experiences a deceleration and re-acceleration as approaching Cell#1 and Cell#4. $\bar{U}_y$ of flow developing from SBL and SBR also accelerates after detaching from side baffles. Two peaks of k of the flow developing from the upper portion of primary heat exchangers are caused by the turbulence jet and have values of 10 to 17 m^2/s^2, while the peak of k with a value of 12 m^2/s^2 at downstream of SBL and SBR is due to the vortex shedding (Fig. 9F).

In the outlet duct, flow is from down to up in the center of the duct and reverse flow exists at both sides. $\bar{U}_x$ has higher value at downstream of SBL and SBR for $Z = 127$ mm and $Z = 0$ mm plane while the maximum magnitude of $\bar{U}_x$ appears above Cell#2 and Cell#3 for $Z = −127$ mm plane (Fig. 9A). At the center of the outlet, $\bar{U}_y$ with value of −2 to 8 m/s (Fig 9B) has lower peak value than that in the no damper case. $\bar{U}_y$ at $Z = −127$ mm plane also has smaller fluctuation along *X* axis comparing with $\bar{U}_y$ of the other two planes. For all three *Z* planes, k has value lower than 11 m^2/s^2 (Fig. 9C) and is lower than the corresponding *Z* planes of no damper case. It is also noticeable that for $Z = 0$ mm and $Z = −127$ mm plane, k at down stream of SBL and SBR could have a maximum value of 11 m^2/s^2 in outlet duct while k at downstream of Cell#2 and Cell#3 have the maximum value of less than 10 m^2/s^2. The phenomenon suggests that the TKE generated by separation and entrainment would dissipate more quickly while TKE generated by vortex shedding exists at further downstream in outlet duct.

The smaller peak value of $\bar{U}_y$ in three planes for open damper case suggests lower flow rate comparing with that in no damper case.

3.3 Highly Restricted Damper Case

As the inlet damper is highly restricted, the flow fields of three *Z* planes are asymmetric for both the mean velocity (*X*-component and *Y*-component) and TKE, as shown in Fig. 10.

Although $\bar{U}_x$ and k stay at a low value of −1 to 1 m/s (Fig. 11G) and 0 to 2 m^2/s^2 (Fig. 11H) below $Y = 350$ mm, respectively, similar with that in no damper case and open damper case, $\bar{U}_y$ with maximum of 2.5 m/s drops a lot comparing with the other two cases and negative value is found between SBR and Cell#1 for all three *Z* planes. Moreover, negative $\bar{U}_y$ appears at Cell#1 and Cell#2, as well as Cell#2 and Cell#3 for $Z = 127$ mm plane.(Fig. 11H)

The flow between $Y = 370$ mm and $Y = 460$ mm shows more asymmetric pattern while separation bubbles still exist above the upper portion of cells. The maximum magnitude of $\bar{U}_x$ in Figs. 10ADG appears at the tip of SBL. The maximum $\bar{U}_y$ appears at the interval of SBL and Cell#4 and is 5 m/s for $Z = −127$ mm and $Z = 0$ mm plane and 4 m/s

for $Z = 127mm$ plane (Figs. 10BEH). The maximum $\bar{U}_y$ between primary heat exchanger cells decreases as X position is increasing and finally goes down to 1 m/s at the minimum interval between Cell#1 and SBR for $Z = 127$ mm and $Z = 0$ mm plane. $\bar{U}_y$ even becomes negative at the interval of Cell#1 and Cell#2 and the interval of Cell#1 and SBR for $Z = -127$ mm plane (Fig. 11E). Also, the jet flow developing from two adjacent cells towards to left side, the strongest jet flow produced by SBL and Cell#4, which is due to the low pressure above SBL and Cell#4 caused by high velocity. Despite k is lower than 3 m^2/s^2, the pattern of peaks due to vortex shedding and separation is significant.

In the outlet duct, more reverse flow is observed at right side for all three Z planes. Maximum $\bar{U}_y$ appears at the downstream of SBL and Cell#4 and decreases to negative value as going to positive X position smoothly for all three Z planes(Fig. 11B). k shows similar characteristic to $\bar{U}_y$ that has peak value at downstream of SBL and Cell#4 and drops to 0 at right side.

4. CONCLUSIONS

In the present work, PIV was employed to measure the isothermal flow around the primary heat exchanger of a residential gas furnace. Three conditions with different differential pressure of the inlet and outlet of the furnace were tested.

In all three conditions, the similarities between three measured planes suggest the flow between three planes could be approximate uniform along Z direction. The flow is symmetric as the differential pressure between the inlet of the furnace and the outlet of the furnace is low. In such conditions, the maximum $\bar{U}_x$ appears at the tip of two side baffles while the maximum $\bar{U}_y$ appears at the smallest cross section. The flow would then separate from the upper portion of primary heat exchanger cells and become turbulence jet flow. High Turbulence Kinetic Energy is found at the boundary of turbulence jet due to entrainment and downstream of side baffles due to vortex shedding. Though both no damper case and open damper case show similar characteristics, open damper case would have lower flow rate than that of no damper case. As differential pressure between the inlet and the outlet of furnace goes higher and finally approach its maximum as the inlet damper is highly restricted, the internal flow as well as the flow in the outlet duct would transit to asymmetric. The maximum $\bar{U}_y$ appears at the interval of the SBL and Cell#4. The jet flow at right side has lower velocity and Turbulence Kinetic Energy. In the outlet duct, the direction of main flow is from right to left. Multiple reasons can lead to the asymmetric pattern in the highly restricted damper case:(i) The asymmetric structure of the blower. (ii) The opening offset of the blower exit. (iii) The restriction configuration of the inlet (iv) The restriction configuration of the outlet. The experimental results can be helpful to validate CFD work of a residential gas furnace and optimize the design of the next generation gas furnace.

Future work could be done to study the flow field at the inlet and exit of the blower and the flow filed paralleling to YZ plane. Moreover, the flow field considering heat transfer should be studied.

ACKNOWLEDGEMENT

REFERENCES

https://catalog.data.gov/dataset/buildings-energy-data-book-6d4d2.

Adrian, R. J. & Westerweel, J. (2011). *Particle image velocimetry*. Cambridge University Press.

Chwalowski, M., Didion, D. A. & Domanski, P. A. (1989). Verification of evaporator computer models and analysis of performance of an evaporator coil. *Ashrae Transactions*, 95(1), 1229-1236.

Kamiji, Y., Terada, A. & Sugiyama, H. (2012). Experimental study of airflow-mixture in hvac unit by using piv. *Journal of Energy and Power Engineering*, 6(1), 41-48.

Raffel, M., Willert, C. E., Wereley, S. & Kompenhans, J. (2007). *Particle image velocimetry: A practical guide, 2nd edition*. Heidelberg, Springer.

Yashar, D. A. & Domanski, P. A. (2009). Particle image velocimetry measurements and cfd-based predictions of air distribution at evaporator inlet and outlet. Technical report.
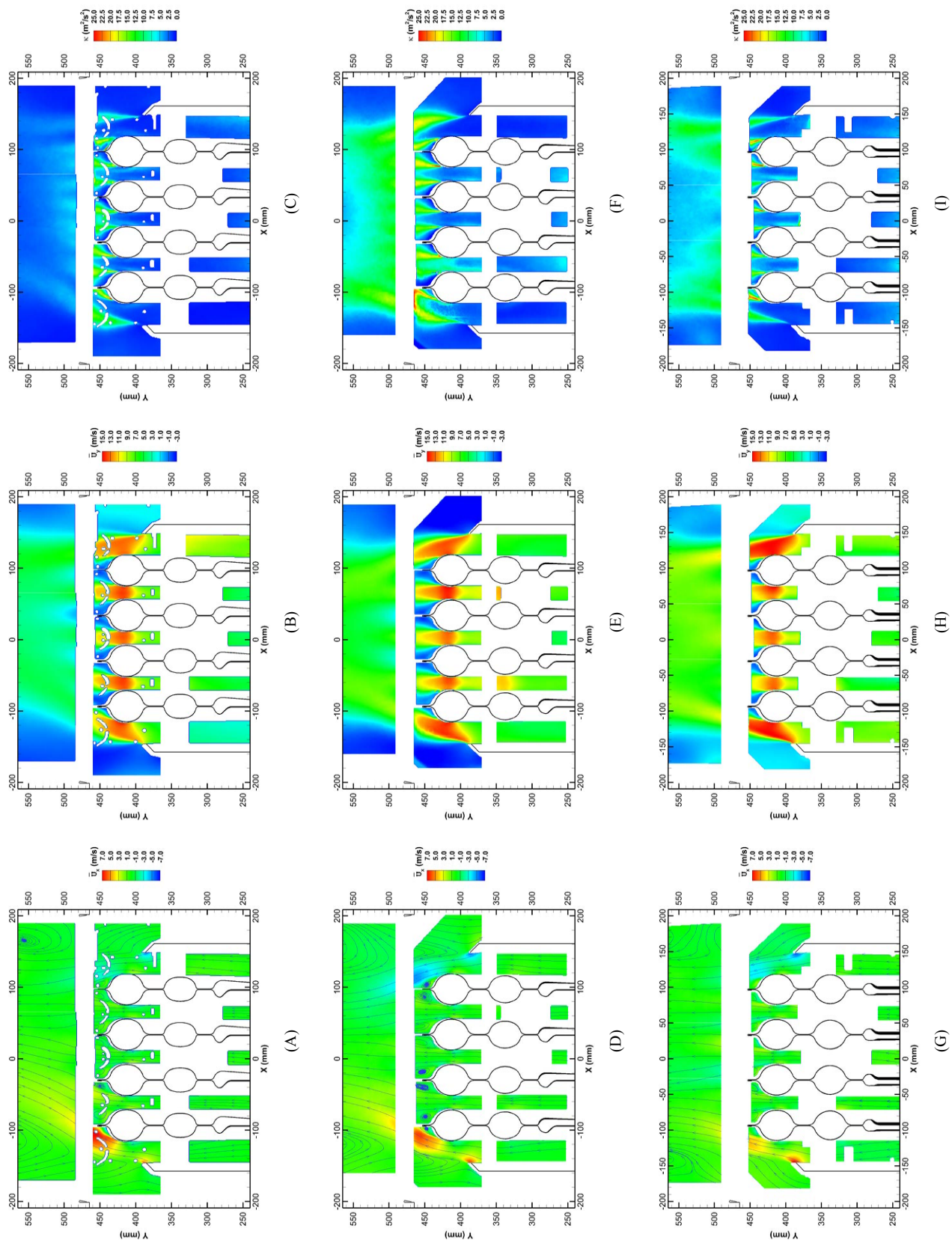
Figure 6: Mean velocity and TKE of three planes at no damper case. (A) $\bar{U}_x$ **& streamline at** $Z = 127\ mm$; **(B)** $\bar{U}_y$ **& streamline at** $Z = 127\ mm$; **(C)** k **at** $Z = 127\ mm$; **(D)** $\bar{U}_x$ **& streamline at** $Z = 0\ mm$; **(E)** $\bar{U}_y$ **at** $Z = 0\ mm$; **(F)** k **at** $Z = 0\ mm$; **(G)** $\bar{U}_x$ **& streamline at** $Z = -127\ mm$; **(H)** $\bar{U}_y$ **at** $Z = -127\ mm$; **(I)** k **at** $Z = -127\ mm$.
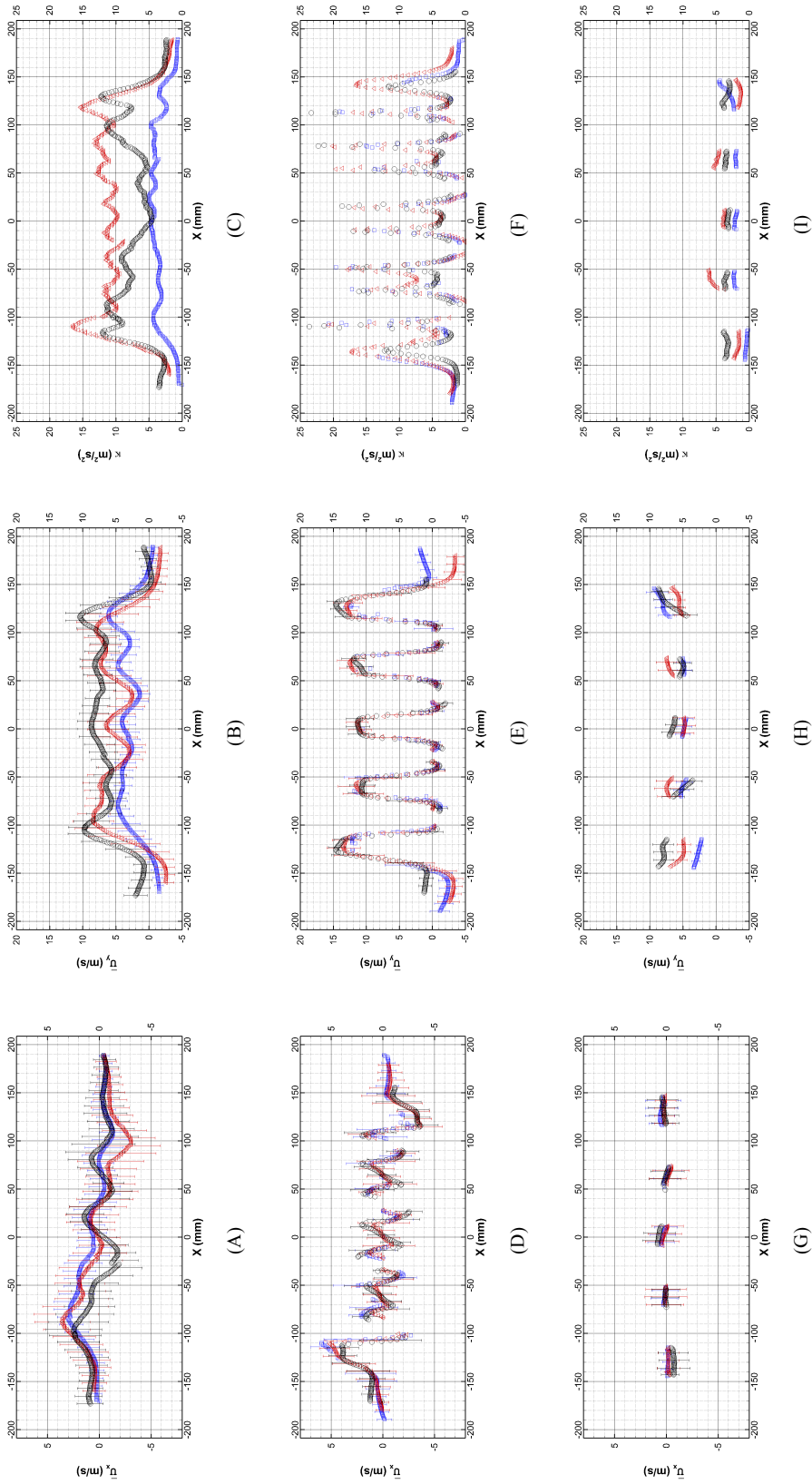
Figure 7: Profile of mean velocity with RMS and TKE of three planes at no damper case. (A) $\bar{U}_x$ at $Y = 500\ mm$; **(B)** $\bar{U}_y$ at $Y = 500\ mm$; **(C)** k at $Y = 500\ mm$; **(D)** $\bar{U}_x$ at $Y = 440\ mm$; **(E)** $\bar{U}_y$ at $Y = 440\ mm$; **(F)** k at $Y = 440\ mm$; **(G)** $\bar{U}_x$ at $Y = 260\ mm$; **(H)** $\bar{U}_y$ at $Y = 260\ mm$; **(I)** k at $Y = 260\ mm$; **Blue Square:** $Z = 127\ mm$; **Red Triangle:** $Z = 0\ mm$; **Black Circle:** $Z = -127\ mm$. (The origin data was bi-cubic interpolated to get data at integral positions, only 1/2 of the velocity & TKE data and 1/16 of the RMS data are plotted for clarity of display)
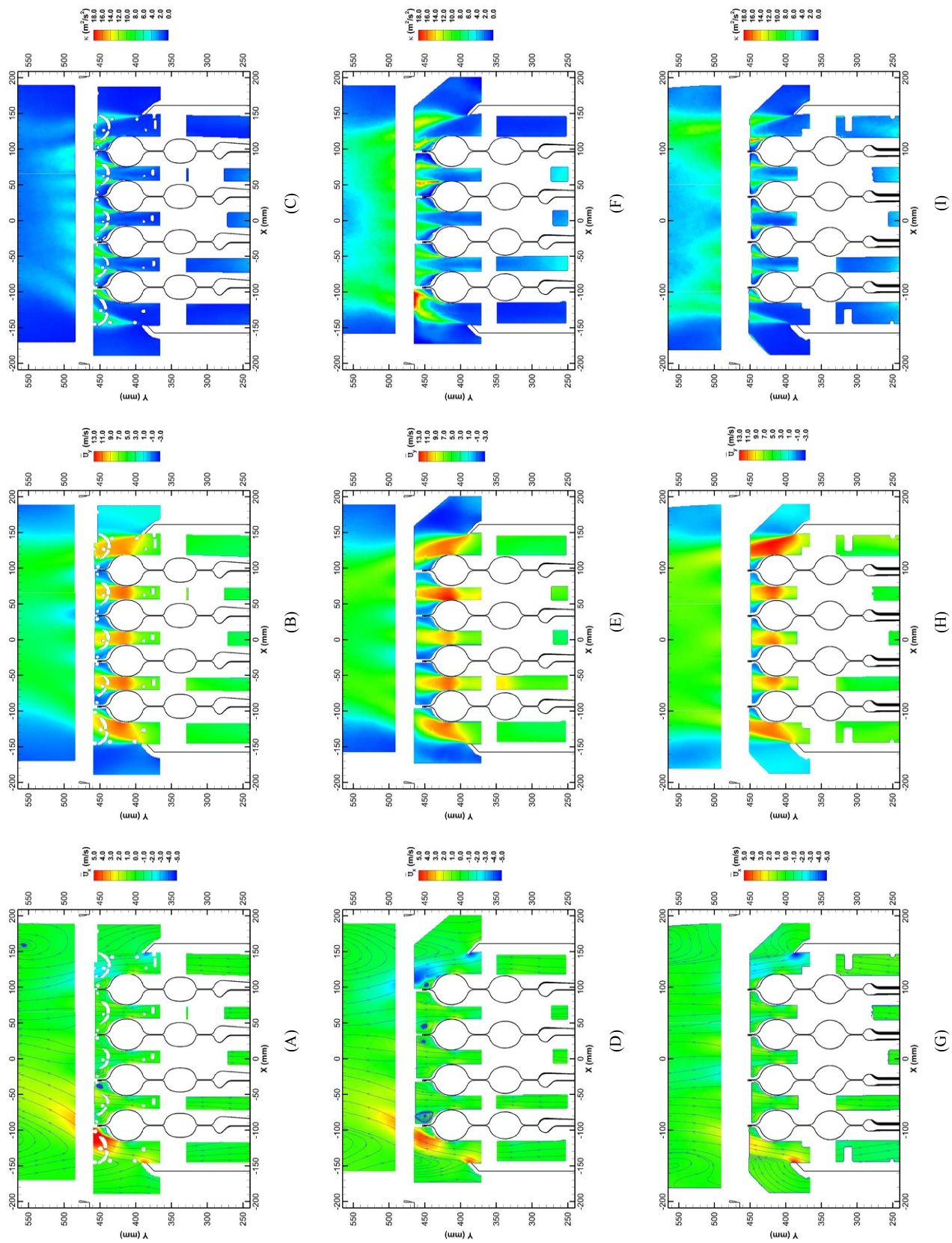
Figure 8: Mean velocity and TKE of three planes at open damper case. (A) $\bar{U}_x$ **& streamline at** $Z = 127\ mm$; **(B)** $\bar{U}_y$ **at** $Z = 127\ mm$; **(C)** k **at** $Z = 127\ mm$; **(D)** $\bar{U}_x$ **& streamline at** $Z = 0\ mm$; **(E)** $\bar{U}_y$ **at** $Z = 0\ mm$; **(F)** k **at** $Z = 0\ mm$; **(G)** $\bar{U}_x$ **& streamline at** $Z = -127\ mm$; **(H)** $\bar{U}_y$ **& streamline at** $Z = -127\ mm$; **(I)** k **at** $Z = -127\ mm$
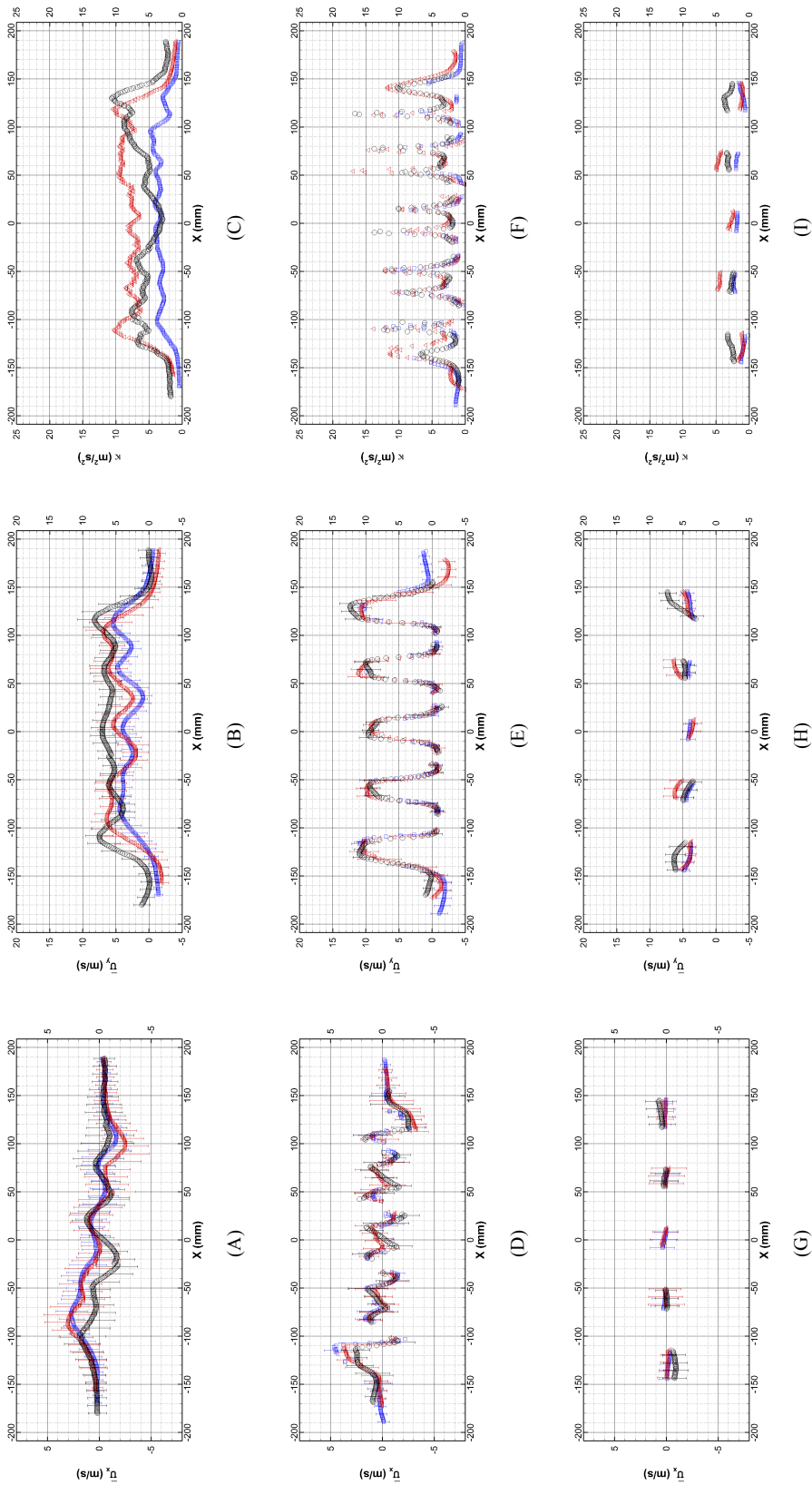
Figure 9: Profile of mean velocity with RMS and TKE of three planes at open damper case. (A) $\bar{U}_x$ at $Y = 500$ *mm*; **(B)** $\bar{U}_y$ at $Y = 500$ *mm*; **(C)** k at $Y = 500$ *mm*; **(D)** $\bar{U}_x$ at $Y = 440$ *mm*; **(E)** $\bar{U}_y$ at $Y = 440$ *mm*; **(F)** k at $Y = 440$ *mm*; **(G)** $\bar{U}_x$ at $Y = 260$ *mm*; **(H)** $\bar{U}_y$ at $Y = 260$ *mm*; **(I)** k at $Y = 260$ *mm*; **Blue Square:** $Z = 127$ *mm*; **Red Triangle:** $Z = 0$ *mm*; **Black Circle:** $Z = -127$ *mm*. (The origin data was bi-cubic interpolated to get data at integral positions, only 1/2 of the velocity & TKE data and 1/16 of the RMS data are plotted for clarity of display)
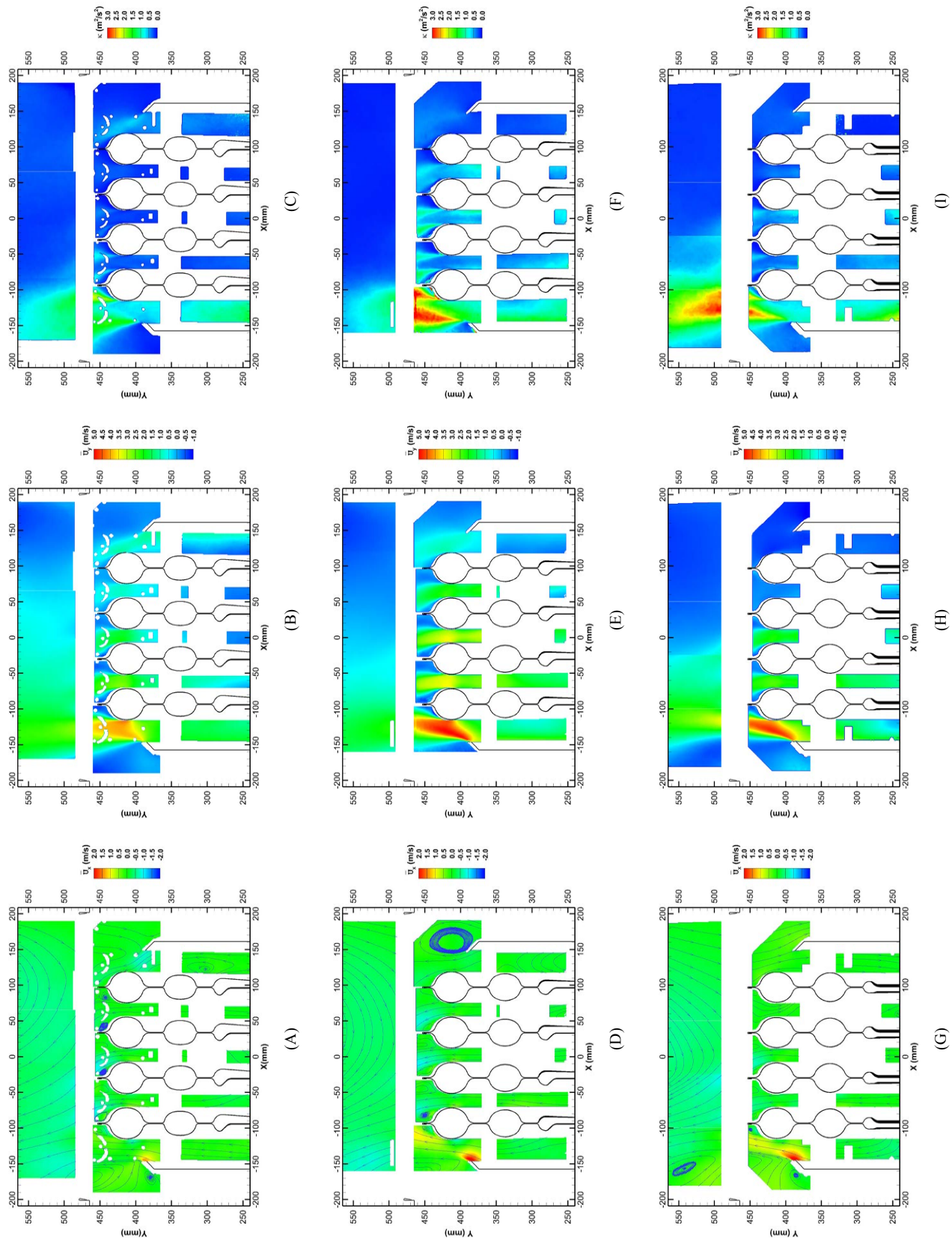
Figure 10: Mean velocity and TKE of three planes at highly restricted damper case. (A) $\bar{U}_x$ **& streamline at** $Z = 127$ *mm*; **(B)** $\bar{U}_y$ **at** $Z = 127$ *mm*; **(C)** k **at** $Z = 127$ *mm*; **(D)** $\bar{U}_x$ **& streamline at** $Z = 0$ *mm*; **(E)** $\bar{U}_y$ **at** $Z = 0$ *mm*; **(F)** k **at** $Z = 0$ *mm*; **(G)** $\bar{U}_x$ **& streamline at** $Z = -127$ *mm*; **(H)** $\bar{U}_y$ **at** $Z = -127$ *mm*; **(I)** k **at** $Z = -127$ *mm*.
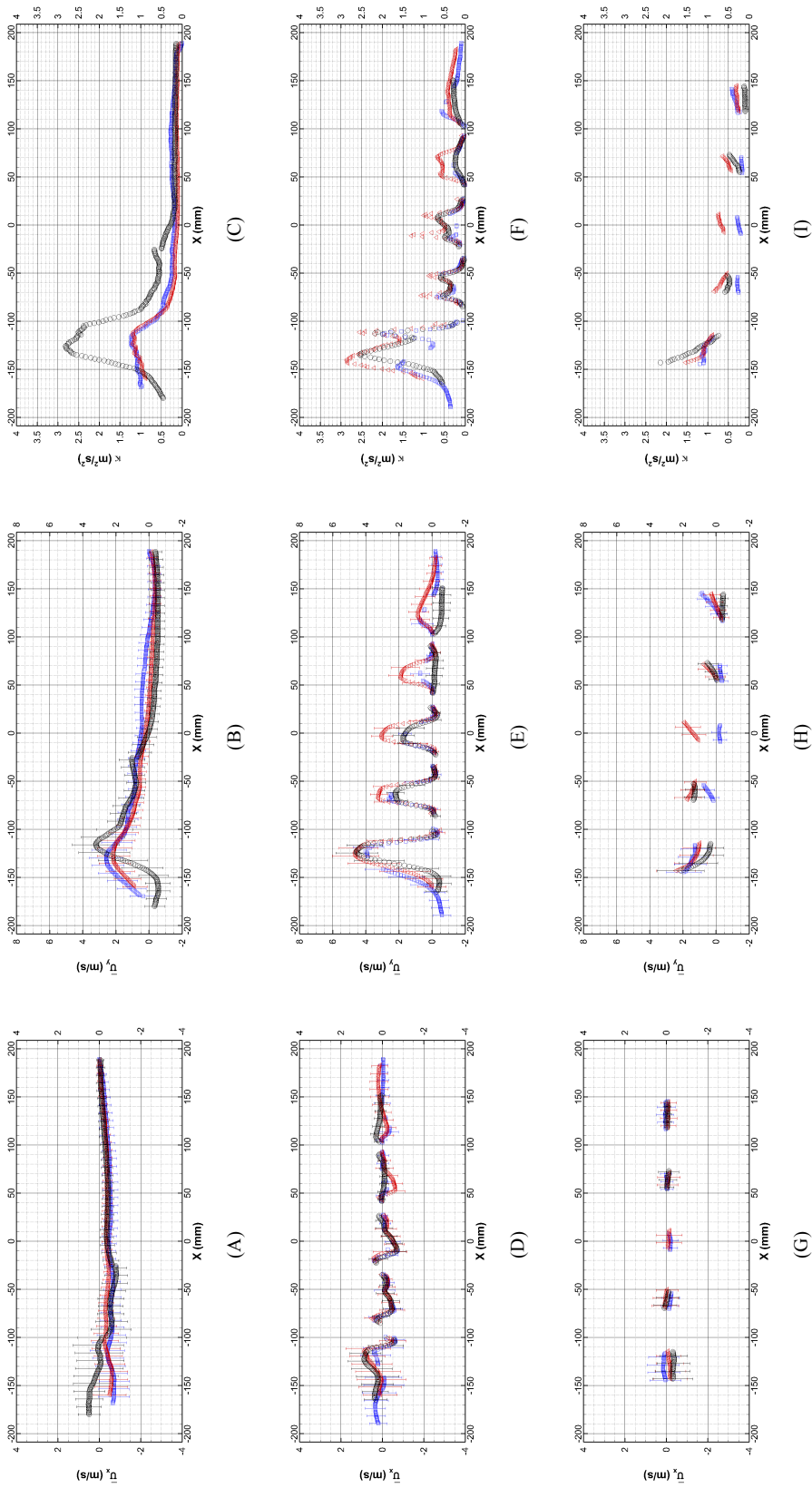
Figure 11: Profile of mean velocity with RMS and TKE of three planes at highly restricted damper case. (A) $\bar{U}_x$ at $Y = 500$ *mm*; **(B)** $\bar{U}_y$ at $Y = 500$ *mm*; **(C)** k at $Y = 500$ *mm*; **(D)** $\bar{U}_x$ at $Y = 440$ *mm*; **(E)** $\bar{U}_y$ at $Y = 440$ *mm*; **(F)** k at $Y = 440$ *mm*; **(G)** $\bar{U}_x$ at $Y = 260$ *mm*; **(H)** $\bar{U}_y$ at $Y = 260$ *mm*; **(I)** k at $Y = 260$ *mm*; **Blue Square:** $Z = 127$ *mm*; **Red Triangle:** $Z = 0$ *mm*; **Black Circle:** $Z = -127$ *mm*. **(The origin data was bi-cubic interpolated to get data at integral positions, only 1/2 of the velocity & TKE data and 1/16 of the RMS data are plotted for clarity of display)**